Effect of welding heat input on microstructure and impact toughness in CGHAZ of X100Q steel

Hui-bin Wang[1,2] · Fei-long Wang[1,3] · Gen-hao Shi[1,3] · Yu Sun[1,2] · Jiang-cheng Liu[2] · Qing-feng Wang[1,3] · Fu-cheng Zhang[1,3]

Abstract

The coarse-grained heat-affected zones (CGHAZs) of X100Q steel were reproduced via simulating their welding thermal cycles with the varying heat input (E_j) from 10 to 55 kJ/cm in Gleeble3500 system. The microstructures were characterized, and the impact toughness was estimated from each simulated sample. The results indicate that the microstructure in each simulated CGHAZ was primarily constituted of lath-like bainite. With the decreased heat input and accordingly the lowered A_{r3} (the onset temperature for this transition), the prior austenite grain and the bainitic packet/block/lath substructure were refined remarkably, and the impact toughness was enhanced due to the microstructure refinement. The bainitic packet was the microstructural unit most effectively controlling the impact properties in CGHAZ of X100Q steel, due to their close correlation with the 50% fracture appearance transition temperatures, their size equivalent to the cleavage facet and their boundaries impeding the crack propagation.

Keywords X100Q bainitic steel · Coarse-grained heat-affected zone · Impact property · Bainitic substructure · Fractography

1 Introduction

Low-C V–Nb–Ti-microalloyed bainitic steel X100Q has been increasingly required for welding fabrication of crucial structures, such as high-pressure pipeline, heavy jack-up leg and large-sized construction machinery. Great efforts have been made for decades to achieve comprehensive performance of high strength and good toughness in the base metal and welded joint, via reasonably designing the alloying compositions and fabrication procedures for yielding an optimal microstructure accordingly [1–9]. This optimized microstructure usually consisted of finer-grained bainitic ferrite [10, 11], denser dislocations, finer precipitates and more dispersed martensite/austenite (M/A) constituent [12, 13].

Among these efforts, the impact properties of coarse-grained heat-affected zone (CGHAZ) in such a high-strength steel have recently received more attentions [14–16], since the welding thermal cycles of this steel might result in a coarse-grained microstructure with brittle phase, and a degraded toughness in this local zone [3, 14].

Some efforts have also been made to estimate the correlation between this microstructure and the final impact properties in CGHAZ [17–19]. The microstructure in CGHAZ of such a high grade steel normally comprises lath bainite (LB), granular bainite (GB) and M/A constituent [20, 21]. Especially for lath bainitic or martensitic steel, the prior austenite grain (PAG) could be divided into the packets and one packet could be redivided into the blocks [22–24]. PAG was assumed to be an effective microstructure unit controlling the toughness of bainitic steel, and in contrast, the microcrack could propagate directly across the packet boundaries [25, 26]. However,

✉ Qing-feng Wang
  wqf67@ysu.edu.cn

1 State Key Laboratory of Metastable Materials Science and Technology, Yanshan University, Qinhuangdao 066004, Hebei, China

2 Technical Center, Tianjin Pipe (Group) Co., Ltd., Tianjin 300301, China

3 National Engineering Research Center for Equipment and Technology of Cold Strip Rolling, Yanshan University, Qinhuangdao 066004, Hebei, China

according to Refs. [24, 27], the packet could act as a microstructure unit effectively controlling the impact toughness due to their boundaries hindering the cleavage crack propagation. You et al. [28] even attributed a tough CGHAZ to an optimized packet substructure with high-angle grain boundary (HAGB, with crystallographic misorientation angle above 15°), and the dispersed M/A constituent in small size. In contrast, the block was recently supposed to be the minimum substructure unit in control of toughness [29]. Therefore, there still exist different and even contradictory opinions on the correlation between the bainitic structure and the impact properties. In order to precisely analyze and greatly enhance the toughness in welded joint, it is essential to understand this correlation and clarify the effective bainitic substructure unit governing the impact toughness of CGHAZ. The corresponding efforts, however, have been rarely reported until recently, to the knowledge of authors.

As such, CGHAZs of a X100Q bainitic steel with different welding heat input (E_j) were reproduced via a Gleeble3500 system, for the quantitative estimations of their microstructure and impact properties. The correlations among the welding heat input, the microstructure and the impact properties were emphasized, and the effective bainitic substructure unit governing the impact properties of CGHAZ was clarified.

2 Experimental material and procedure

A 20-mm-thick X100Q commercial steel tube with chemical compositions listed in Table 1 was used for the present attempt. This steel was microalloyed with 0.06 wt.% V, 0.03 wt.% Nb and 0.02 wt.% Ti, for providing a forceful pinning impact on the migrating grain boundary in the processes including the billet reheating, rolling, quenching, tempering and subsequent welding [30]. The as-received microstructure of this steel is presented in Fig. 1, which consisted of LB, GB and M/A constituent.

The cuboid-shaped samples of 11 mm × 11 mm × 80 mm in size were sectioned from the steel tube along the longitudinal direction. For preparing CGHAZ samples with E_j of 10, 25, 40 and 55 kJ/mm, the single-pass welding thermal cycle curves were programmed through Rykalin two-dimensional heat transfer model and simulated in a
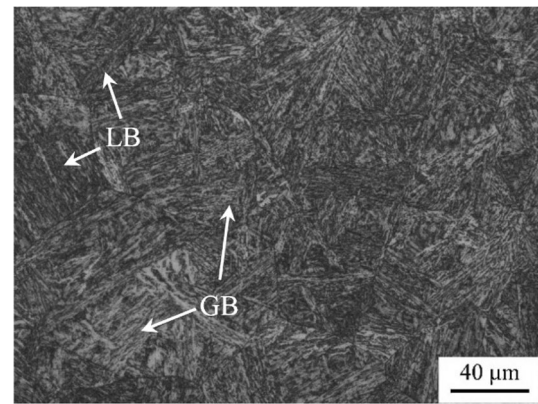
Table 1 Chemical composition of experimental steel (wt.%)

C	Si	Mn	Ni	Cr	Mo	V	Nb	Ti	Fe
0.12	0.25	1.14	0.5	0.43	0.33	0.06	0.03	0.02	Balance

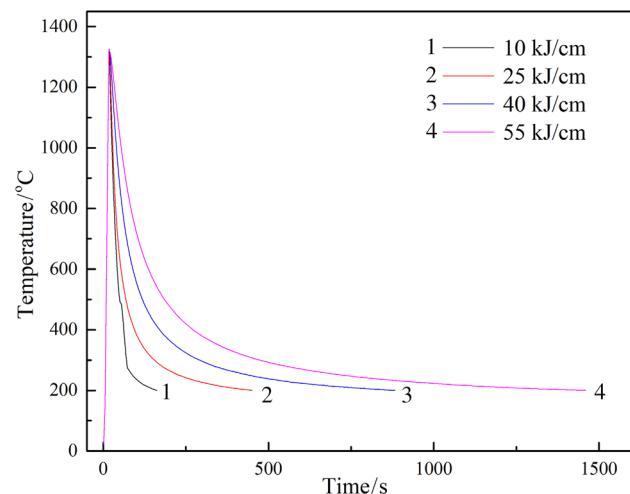**Fig. 1** Typical optical micrograph of as-received X100Q steel

Fig. 2 Welding thermal cycles for simulating CGHAZs in experimental steel welded with different E_j

Gleeble-3500 system. As indicated in Fig. 2, the samples were processed via heating to 1350 °C at 100 °C/s, soaking for a duration of 0.5 s, and subsequently cooling to room temperature at the different cooling time from 800 to 500 °C, $t_{8/5}$, of 15, 31, 60 and 102 s, for satisfying the respective welding heat input. Four samples containing an identical CGHAZ were made for each welding heat input: one for microstructure characterization and three for Charpy V-notch impact testing.

After the simulation, the sample for microstructure observations was wire-cut along the plane perpendicular to the axis of sample, where the thermocouple were positioned. The samples were polished and etched in a 4 vol.% Nital solution. Then, the samples were examined via the optical microscope (Axiover-200MAT, Göttingen, Germany) and further via the scanning electron microscope (SEM, Hitachi S-3400, Hitachi, Japan) to observe the morphology of PAG and bainitic packet. Moreover, the characteristics of M/A constituent, ferrite plates and dislocation in the samples were determined using a

transmission electron microscope (TEM, JEM-2010, Tokyo, Japan). Furthermore, the distributions of grain boundary misorientation angle and HAGB were characterized through electron back-scattered diffraction (EBSD, TSL-EBSD, Tokyo, Japan). After the bainitic packet was identified from SEM micrograph and delimited according to its morphological feature, the packet size was given by $l = \sqrt{l_1 l_2}$, where l_1 and l_2 are the average packet length and width, respectively. The packet size was taken as the average value of at least 50 measured packets from more than 20 SEM images. The bainitic block was identified through EBSD inverse pole figure according to its crystallographic feature. The quantitative estimation of block width was performed with line intercept method using the Image-Pro Plus software (Media Cybernetics, Rockville, MD, USA). To reduce the error, at least 200 crystallographic blocks from more than five EBSD inverse pole figures for each CGHAZ sample were included in statistical estimation, and the average value was reported.

CGHAZ simulation sample was further machined into the standard Charpy V-notch sample of 10 mm × 10 mm × 55 mm in size, with the notch machined at the position of the thermocouple, for the impact property estimation. In addition, 50% fracture appearance transition temperatures (FATT$_{50\%}$) was determined through a set of impact experiments at different temperatures from 20 to − 80 °C, and typical impact fracture surfaces were observed using SEM in order to analyze the difference in cleavage facet morphology.

3 Results

3.1 Microstructure of simulated CGHAZ

Typical SEM observations of the microstructure in each CGHAZ with different E_j are presented in Fig. 3, and their microstructural feature quantifications including PAG and bainitic packet size are summarized in Table 2. The microstructure in each CGHAZ sample consisted of predominant LB and a small amount of GB, irrespective of E_j. Additionally, PAG could be divided into several bainitic packets, which were delimited with the black lines, and the island-like M/A constituent was dispersed in PAG and bainitic ferrite boundaries. With the decreasing E_j, LB increases at the expense of GB. Furthermore, PAG and bainitic packet were gradually refined (Fig. 3), owing to the decreased E_j, and their average sizes (PAG size D_γ and packet size D_P) decreased from 59.8 to 19.2 μm and from 37.5 to 12.1 μm, respectively, whereas the area fraction of M/A constituent, $f_{M/A}$, decreased from 6.7 to 2.7% (Table 2).

M/A packet could be further subdivided into the martensitic/bainitic block substructure, which was defined as a group of bundled laths with the same orientation, according to Refs. [22–24]. Recently, the block substructure was successfully depicted through EBSD technique [31]. Their boundaries were classified as HAGBs and characterized by the misorientation angle higher than 15° [24]. PAG/packet/block boundaries in each CGHAZ were identified from their crystallographic features through the band contrast (BC) map (Fig. 4a) and the inverse pole figure (IPF, Fig. 4b–d). The "line method" was applied on IPF, as shown in Fig. 4b, in order to explore the misorientation angle between PAG/packet/block boundaries (Fig. 4e). This method has been extensively applied in previous works, such as in Ref. [27]. As shown in Fig. 4e, the misorientation angle distribution between the boundaries of PAG/packet/block in sixty randomly selected groups indicated distinctly that the misorientation angle between the boundaries of PAG/packet/block ranged from 18°/15°/7° to 62°/55°/27°, with the average value of 58°/46°/24° as a typical one (Fig. 4f). The result was quite similar to those data recently reported by Wang et al. [31]. The bainitic block was indicated by the arrows in Fig. 4b, and the average block width W_B for each CGHAZ was determined, as demonstrated in Table 2. As Table 2 shows, W_B decreased from 14.8 to 5.4 μm with the decreasing E_j from 55 to 10 kJ/cm, indicating that the bainitic block was also refined evidently.

Typical TEM observations of the microstructure in CGHAZ with the different E_j of 55, 40 and 25 kJ/cm are demonstrated in Figs. 5 and 6, respectively. There were two types of bainitic ferrite by their morphologies: plate and block. This plate-/block-like bainitic ferrite possessed the relatively high-/low-density dislocations and could be categorized as LB/GB, according to Bhadeshia and Christian [32]. In contrast, CGHAZ with $E_j = 25$ kJ/cm predominately contained the plate-like bainitic ferrite (Fig. 6c), that is, LB. Therefore, LB increased and GB decreased with the decreasing E_j, and accordingly the amount of dislocations also increased. In addition, the bainitic lath was thinned significantly, due to the decreased E_j. Furthermore, the bright (Fig. 5c) and dark (Fig. 5d) field images, as well as the selected area diffraction pattern (Fig. 5e), revealed that the island was a constituent phase of martensite and austenite.

3.2 Impact properties of simulated CGHAZ

The Charpy impact energy at − 40 °C for each CGHAZ with differing heat input is displayed in Fig. 7a. As Fig. 7a indicates, the impact energy for CGHAZ with $E_j = 55$ kJ/cm was at a poor level partly due to relatively high amounts of hard and brittle M/A constituent [33, 34]
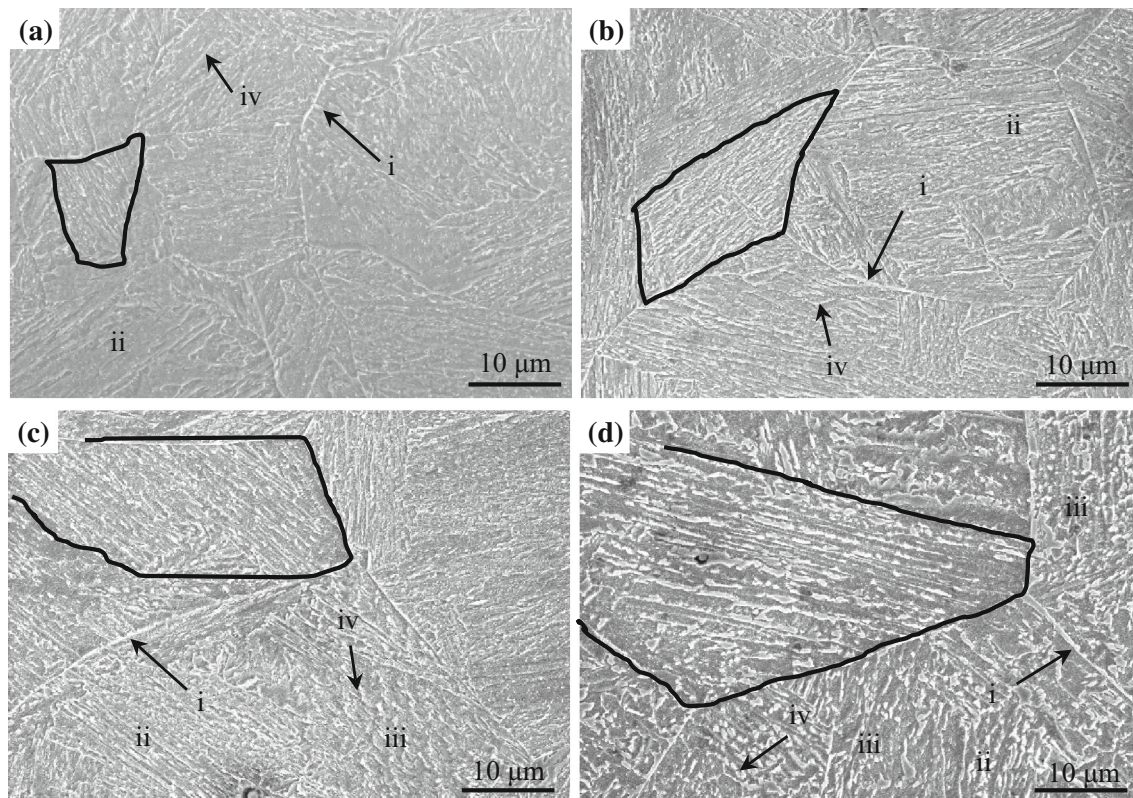
Fig. 3 Typical SEM micrographs of CGHAZ with different E_j of 10 kJ/cm (**a**), 25 kJ/cm (**b**), 40 kJ/cm (**c**) and 55 kJ/cm (**d**) where region surrounded by black lines represented bainitic packets. *i* Prior austenite grain boundary; *ii* LB; *iii* GB; *iv* M/A constituent

Table 2 Quantification results of microstructure and impact fracture surface features

E_j/(kJ cm^{-1})	D_γ/μm	D_P/μm	W_B/μm	$f_{M/A}$/	D_f/μm	FATT$_{50\%}$/°C
10	19.2	12.1	5.4	2.7	13.1	− 71
25	26.4	17.6	9.8	4.2	17.6	− 51
40	41.5	26.2	12.2	5.4	28.8	− 25
55	59.8	37.5	14.8	6.7	38.8	− 18

D_f cleavage facet size

(Table 2). However, it increased slightly with the decreasing E_j from 55 to 40 kJ/cm, mainly owing to the bainitic ferrite refinement (Figs. 3–5 and Table 2). As E_j decreased further to 25 and 10 kJ/cm, the Charpy impact energy was significantly enhanced due to both an even finer bainitic ferrite and even less M/A constituent (Figs. 3–5 and Table 2), also indicating an elevated energy consuming for the initiation and propagation of cleavage crack [35]. The Charpy impact energy at different temperatures from 20 to 80 °C for each CGHAZ with different heat inputs is shown in Fig. 7b. FATT$_{50\%}$ value for each CGHAZ was determined, as summarized in Table 2, indicating that FATT$_{50\%}$ decreased from − 18 to − 71 °C along with the decreasing E_j from 55 to 10 kJ/cm.

The impact fracture surfaces of CGHAZ with different heat inputs were observed and are displayed in Fig. 8. It obviously indicated that the fracture surface in each CGHAZ exhibited a typical cleavage fracture. D_f for each CGHAZ was determined, as summarized in Table 2. D_f decreased remarkably from 38.8 to 13.1 μm with the decrease in heat input from 55 to 10 kJ/cm. Furthermore, apart from the cleavage facet, the secondary crack could also be identified in SEM fractography. Also, as exhibited in Fig. 8, the secondary crack in CGHAZ with a relatively low heat input of E_j = 25 kJ/cm (Fig. 8a) consisted of a larger number of shorter segments, indicating that this finer microstructure (Figs. 3–5 and Table 2) was more effective in resistance to the crack propagation, in comparison with
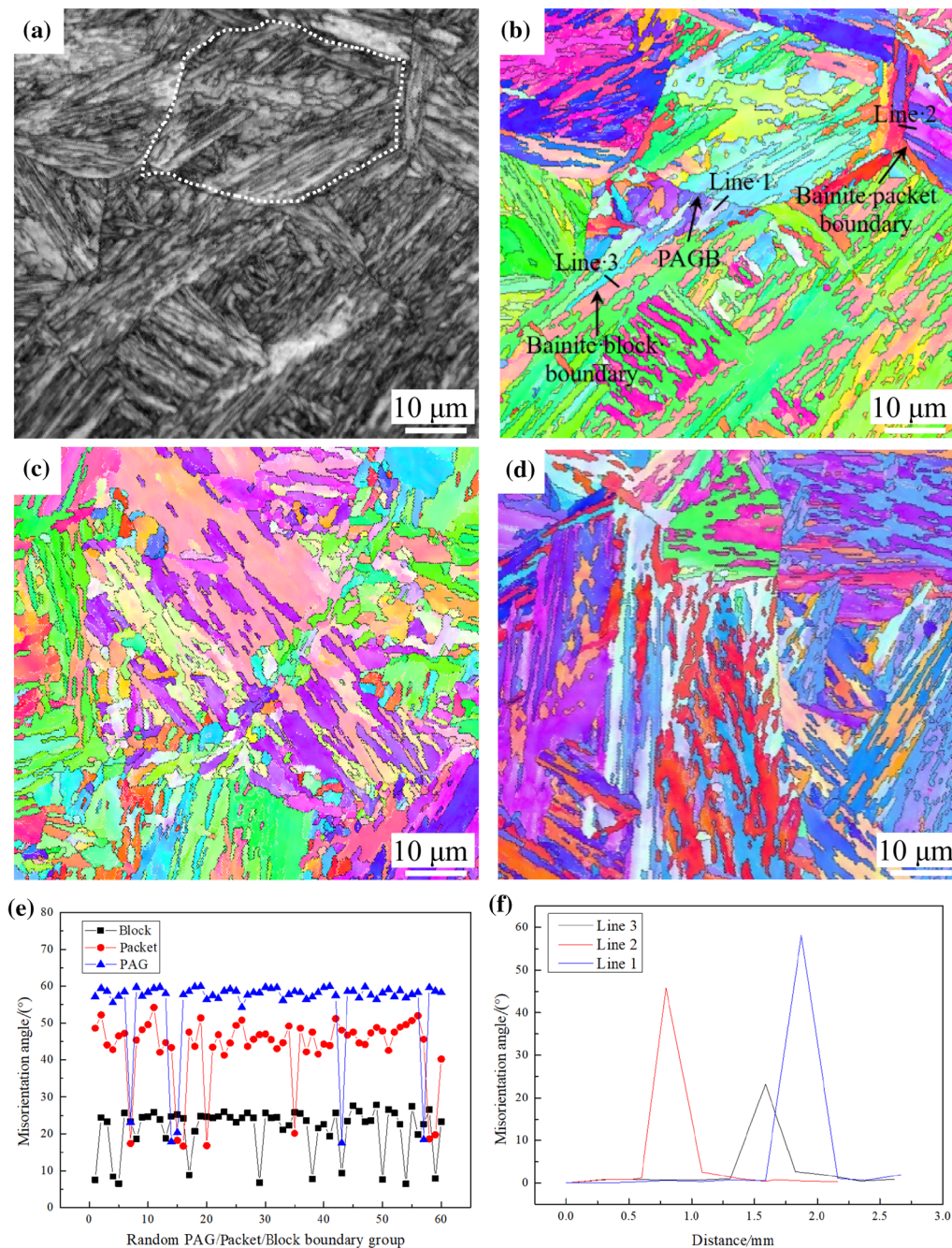
Fig. 4 BC map (**a**) for CGHAZ with E_j = 25 kJ/cm and IPFs for CGHAZ with E_j of 25 (**b**), 40 (**c**) and 55 kJ/cm (**d**) as well as misorientation angle distribution between boundaries of PAG/packet/block (**e**) and their typical misorientation angles (**f**). *PAGB* Prior austenite grain boundary

that in CGHAZ with a medium heat input of E_j = 40 kJ/cm (Fig. 8b) and a high heat input of E_j = 55 kJ/cm (Fig. 8c).

These impact fractured samples were further wire-cut along the plane perpendicular to the fracture surface and etched, for the secondary crack to be estimated in more detail via SEM. As exhibited in Fig. 9, the secondary crack in CGHAZ sample with E_j = 25 kJ/cm, firstly deviated at PAG boundary (indicated by a white arrow in Fig. 9a), then propagated across the bainitic block substructures in an

identical packet (Fig. 9a, b), and finally deflected and terminated at the bainitic boundaries (pointed out by a yellow arrow and a red one, respectively, in Fig. 9a). By contrast, the secondary crack in CGHAZ sample with E_j = 55 kJ/cm, propagated across all the bainitic block boundaries directly without deviation (identified by a white arrow in Fig. 9b), and then was arrested at PAG and the bainitic packet boundaries (pointed out by a yellow arrow and a red one, respectively, in Fig. 9b). Hence, PAG boundary with a
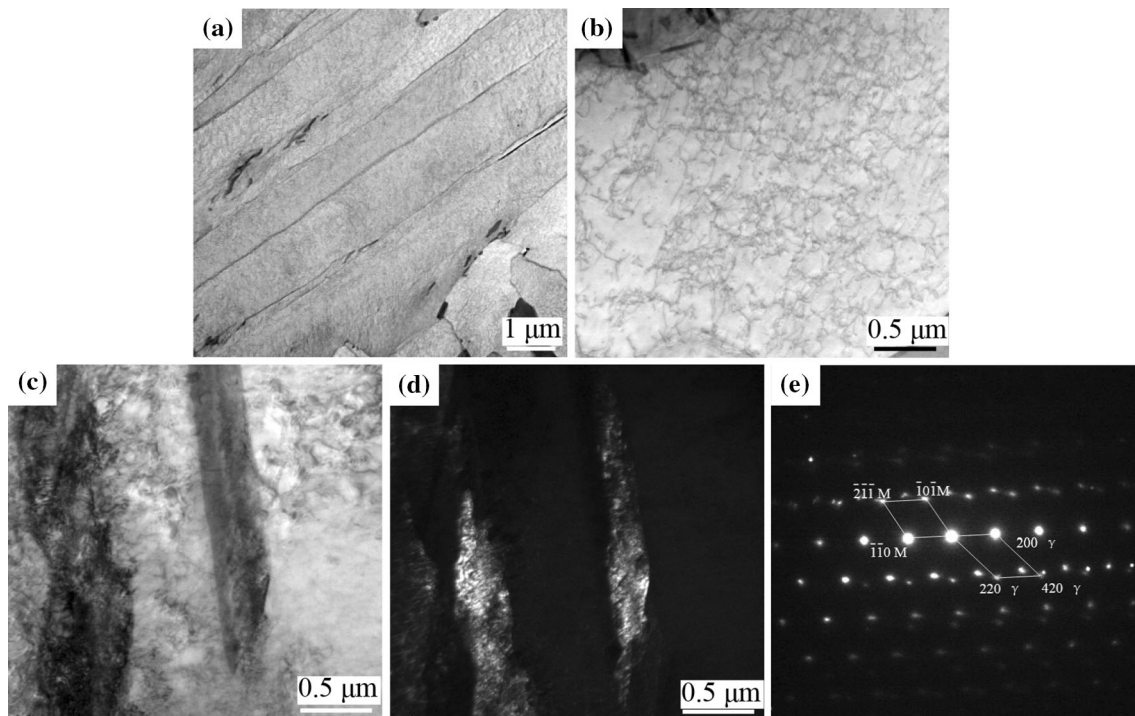
Fig. 5 Typical TEM micrographs of CGHAZ with E_j = 55 kJ/cm, showing plate- and block-like bainitic ferrite (**a**) and their dislocation substructure (**b**), as well as typical M/A constituent indicated by bright field (**c**), dark field (**d**) and selected area diffraction pattern (**e**)
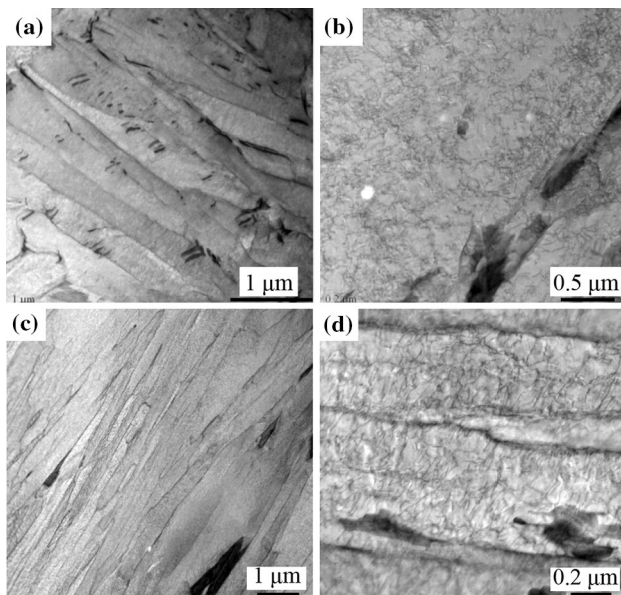

Fig. 6 Typical TEM micrographs of CGHAZ with E_j of 40 kJ/cm (**a**, **b**) and 25 kJ/cm (**c**, **d**), showing plate-like bainitic ferrite (**a**, **c**) and their dislocation substructure (**b**, **d**)

typical misorientation angle of 58° and the packet boundary with a typical misorientation angle of 46° could effectively divert the crack propagation and even arrest the microcrack, and in contrast, the bainitic block boundary with a typical misorientation angle of 24° could not hinder the crack propagation.

4 Discussion

4.1 Effect of welding heat input on microstructure in CGHAZ

CGHAZ microstructure evolution in the welding thermal cycle could be interpreted as follows. The coarse-grained austenite formed in each sample during the reheating and soaking briefly at 1350 °C. During the continuous cooling transition of $\gamma \rightarrow \alpha$ staring from A_{r3} (the onset temperature for this transition), the bainitic ferrite nucleated predominately at PAGB, and γ/α interface moved intragranularly. The expansion curve for the cooling course of welding thermal cycle imposed on each sample was simultaneously measured using a dilatometer, as shown in Fig. 10, and A_{r3} points were determined, as also indicated in Fig. 10, for the effect of welding heat input on CGHAZ microstructure to be further identified.

It is clear that A_{r3} decreased with the decreasing E_j. For understanding their dependence on E_j, D_γ of these samples was determined quantitatively, as summarized in Table 2. With the decreasing E_j, D_γ decreased evidently, and PAG was refined accordingly. This resulted from a shorter dwelling duration at temperature higher than 1200 °C, an enhanced pinning effect of Ti- and Nb-rich carbonitrides on PAG boundaries, and accordingly a restricted γ grain growth [32, 36]. However, a fine-grained PAG commonly
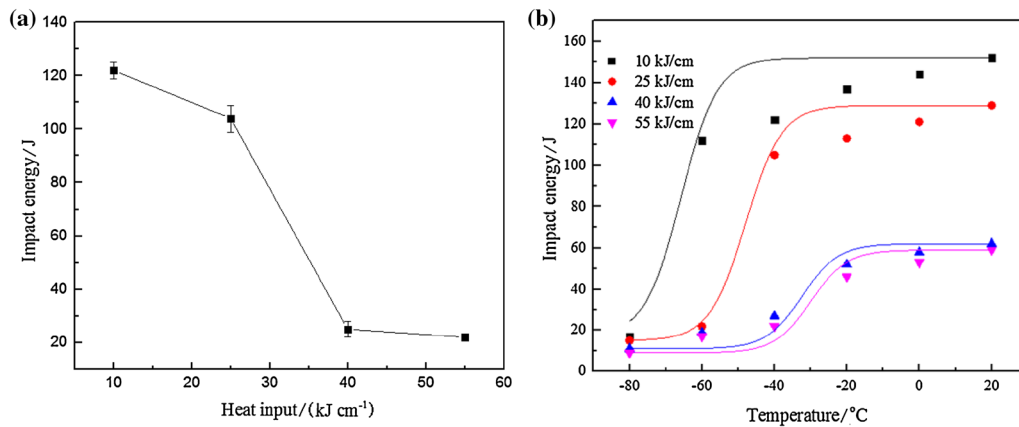
Fig. 7 Charpy impact energy at − 40 °C for CGHAZ sample as function of welding heat input (**a**) and Charpy impact energy at different temperatures (**b**)
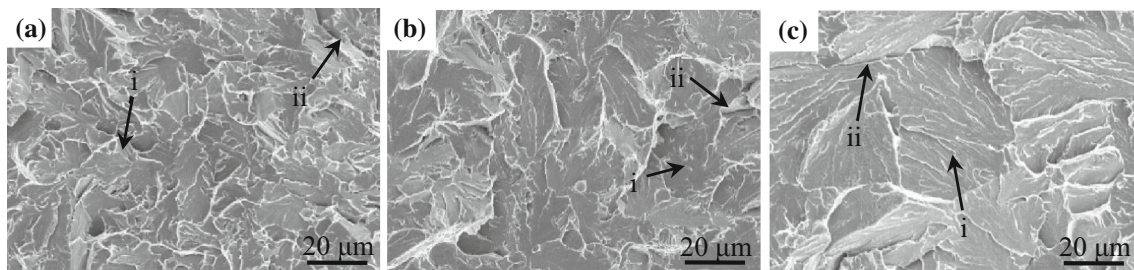

Fig. 8 Typical SEM micrograph of impact fracture surface for CGHAZ with different E_j of 25 (**a**), 40 (**b**) and 55 kJ/cm (**c**). *i* Cleavage facet; *ii* secondary crack
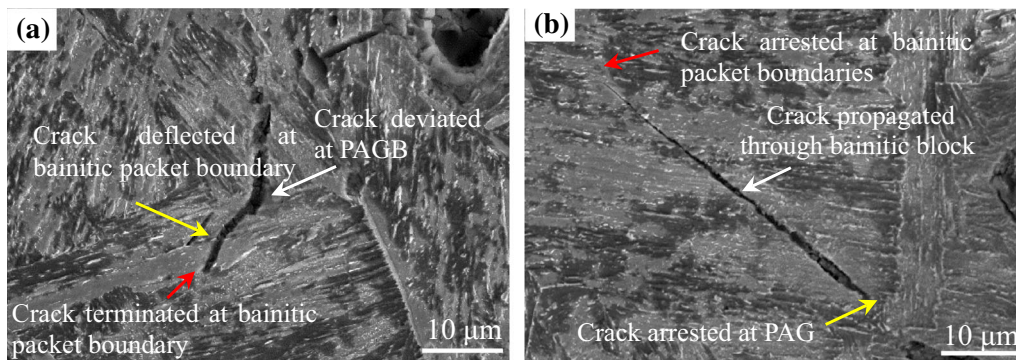

Fig. 9 Morphologies of secondary cracks underneath impact fracture surface. **a** E_j = 25 kJ/cm; **b** E_j = 55 kJ/cm

possessed an increased amount of boundary containing high energy, and in turn supported an elevated A_{r3}. On the other hand, the decreased E_j still normally brought about a lower $t_{8/5}$ or an elevated cooling rate. The diffusion-controlled $\gamma \rightarrow \alpha$ phase transformation including Fe–C atoms diffusion, partition and realignment was thus assumed to be restricted [37]. Accordingly, a decrease in A_{r3} or a super-cooling degree was required to drive the phase transformation. In contrast, a decrease in A_{r3} due to the requirement for further driving the phase transition

predominated an increase in A_{r3} due to PAG refinement. A_{r3} was therefore eventually lowered with the decreasing E_j.

Also, as Fig. 10 shows, CGHAZ with E_j = 55 kJ/cm, had a highest A_{r3} (579 °C), indicating that a phase change of $\gamma \rightarrow GB + LB$ proceeded in this sample at a highest onset temperature. $\gamma \rightarrow GB$ nucleated mainly at PAGB in this sample, and normally preceded $\gamma \rightarrow LB$, according to a previous report [38]; thereby, GB formed in certain amounts, whereas LB mainly nucleated intragranularly
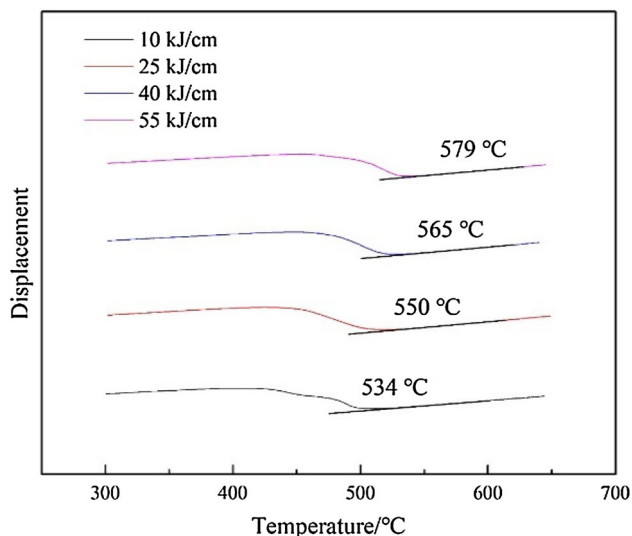
Fig. 10 Expansion curve and A_{r3} measured for each CGHAZ with different E_j

[39], and developed a chief phase in the retained space [17]. However, as A_{r3} decreased to 565, 550 and 534 °C with the decreasing E_j to 40, 25 and 10 kJ/cm, respectively, the driving force for nucleation and growth of intragranular LB increased accordingly, according to Refs. [36, 40–42]. LB, therefore, increased dramatically and finally evolved as a predominant structure in CGHAZ with $E_j = 25$ kJ/cm and $E_j = 10$ kJ/cm.

Of all the samples estimated, CGHAZ with $E_j = 10$ kJ/cm had both the finest PAG and the highest supercooling degree for $\gamma \rightarrow \alpha$ transition, owing to the lowest A_{r3}, as indicated in Fig. 10. This could lead to a highest nucleation rate for this bainitic transition [32, 43] and finally produced a finest bainitic packet/block/lath substructure in this sample. Therefore, all the bainitic packet/block/lath substructure size decreased with the decreasing E_j, due to the lowered A_{r3}, as indicated in Table 2.

Additionally, the dislocation amount for CGHAZ with the different E_j, as actually observed via TEM in Figs. 5 and 6, increased evidently with the decreasing E_j, but in essence, probably depended on A_{r3}. According to Bhadeshia [37], a negative correlation between ρ (the dislocation density for bainite) and B_s (the onset temperature for bainite transition) existed, referring only to B_s in the range from 297 to 647 °C. In this work, A_{r3} for each CGHAZ was included in this range and could satisfy this correlation, indicating an agreement with their estimation.

On the other hand, the amount of M/A constituent increased with the increasing E_j, as shown in Fig. 3 and Table 2. The evolution of M/A constituent fraction with E_j could be explained as follows. During the continuous cooling transition of $\gamma \rightarrow \alpha$, the supersaturated carbon (C) atoms in α diffused toward γ/α interface [44]. Thus, the

untransformed γ became C-enriched and metastable due to C partitioning. The transition of γ' (metastable γ) to bainitic ferrite could proceed conditionally at lower temperatures on cooling, until the retained γ' was considerably stabilized and γ' to bainitic ferrite change became almost impossible thermodynamically, probably due to an extra C-enrichment [45]. The following cooling course could witness M/A constituent formation (Fig. 5); the partial C-enriched γ' transformed to the martensite and retained austenite. Therefore, according to Ref. [12], M/A constituent was a transformed product from γ' on air-cooling, which coexisted with α during the occurrence of $\gamma \rightarrow \alpha + \gamma'$ change normally in a mid-temperature domain. This supposes a close correlation of M/A constituent with γ'. However, γ', was encircled mainly by the granular bainitic ferrite (GBF) and increased with the amount of GBF, due to the increased E_j. Additionally, C atom diffusion from the α to γ' also concurred with $\gamma \rightarrow \alpha + \gamma'$ phase change, leading to γ' with C-enrichment (Figs. 5, 6), as determined from TEM observations. Furthermore, C-enrichment in γ' could increase with the increased E_j, and accordingly enhance their chemical stability. Finally, the increased E_j resulted in an evident increase in the amount of M/A constituent.

4.2 Effect of HAGBs on impact behavior in CGHAZ

Various HAGBs have been extensively accepted as the microstructural unit controlling the toughness of alloys [24, 38, 46], for they store a high energy and can hinder the crack propagation. Accordingly, an increasing amount of HAGBs due to the grain refinement can possess an enhanced toughness. For the present work, there were three kinds of HAGBs in CGHAZ, namely PAGB, bainitic packet and block boundaries. Additionally, all the impact fracture surfaces displayed essentially a cleavage fracture. Therefore, the average cleavage facet size for each CGHAZ was determined and compared to various bainitic structure size (Table 2), for better understanding the correlation between the bainitic structures and impact toughness in CGHAZ.

D_f was compared to D_γ, D_P and W_B, respectively, as shown in Fig. 11, revealing an approximately linear relation between them. Thus, the linear fitting was made and their fitted equations were demonstrated as follows:

$$D_f = 1.01 + 0.64D_\gamma \tag{1}$$

$$D_f = 0.3 + 1.04D_P \tag{2}$$

$$D_f = -4.46 + 2.75W_B \tag{3}$$

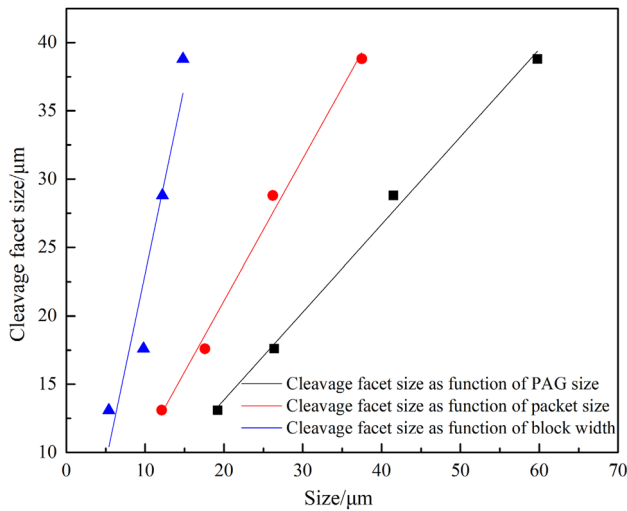The correlation coefficients for Eqs. (1)–(3) were 0.99, 0.98 and 0.85, respectively, indicating a good linear

Fig. 11 Cleavage facet size as functions of D_γ, D_P and W_B

Fig. 12 FATT$_{50\%}$ as functions of D_γ, D_P and W_B

relation between them. PAGB deviated the secondary crack, as identified in Fig. 9a, manifesting an effective hindrance to the crack propagation. However, D_γ was approximately one and a half times D_f, suggesting that PAG might not be the microstructure unit most effectively controlling the impact toughness for CGHAZ samples. Also, the bainitic packet boundaries deviated or arrested the secondary crack, as pointed out in Fig. 9a, indicating that they hindered the crack propagation, the same as PAG did. Simultaneously, D_P was almost equal to D_f, as shown in Table 2. These two factors, the major role in hindering the crack propagation and the quite similar size to the cleavage facet, recommended that the bainitic packet was the microstructure unit most effectively controlling the impact properties of CGHAZ. In addition, the secondary crack propagated across the bainitic block boundaries, as shown in Fig. 9a, b, indicating that the bainite block boundary failed to impede the crack propagation. Moreover, D_f was almost triple as much as W_B. These strongly suggested that the bainite block was not the microstructure unit most effectively controlling the impact behavior in CGHAZ.

For further confirming the roles of PAG and bainitic packet/block substructures in control of the impact toughness for CGHAZ, the Charpy impact energy at temperatures from -80 to 20 °C for each CGHAZ was measured, and their FATT$_{50\%}$ was determined. The relationship between FATT$_{50\%}$ and various bainitic structure size (D) was estimated via the linear fitting of FATT$_{50\%}$ versus $D^{-1/2}$ curve (D referred to D_γ, D_P and W_B), as demonstrated in Fig. 12. Their fitting functions were obtained as follows:

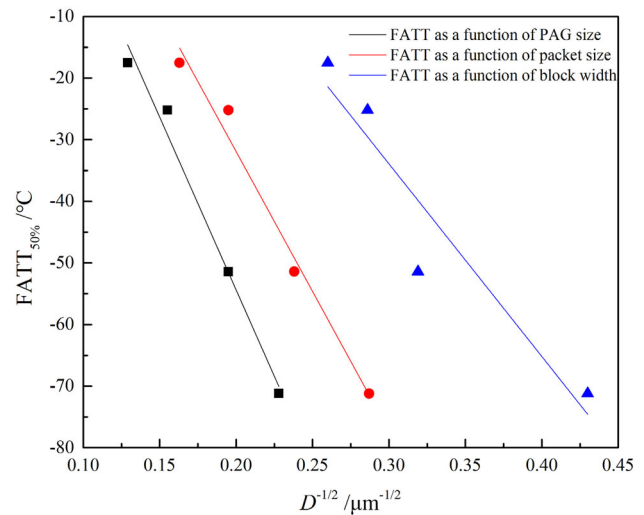$$\text{FATT}_{50\%} = 58 - 561 D_\gamma^{-1/2} \tag{4}$$

$$\text{FATT}_{50\%} = 59 - 454 D_P^{-1/2} \tag{5}$$

$$\text{FATT}_{50\%} = 60 - 313 W_B^{-1/2} \tag{6}$$

The correlation coefficients for Eqs. (4)–(6) were 0.95, 0.98 and 0.86, respectively, also indicating that the bainitic packet, instead of PAG and the bainitic block, was the microstructure unit most effectively controlling the impact properties of CGHAZ.

As such, according to Ref. [24], the fracture stress, σ_f, could be represented as follows:

$$\sigma_f = \left[\frac{4E\gamma_p}{(1-\upsilon^2)d} \right]^{1/2} \tag{7}$$

where E represents the Young's modulus; γ_p is the plastic deformation energy; υ is the Poisson's ratio; and d is the effective grain size, which referred to D_P for the research. σ_f commonly stands for the maximum external stress that the structure can sustain to keep its material from being fractured. The increased σ_f normally implies that the material become more resistant to fracture [24, 38]. D_P decreased significantly (Table 2) with the decreasing E_j, leading to an obvious increase in σ_f. Therefore, with the decreased E_j, the impact toughness was enhanced (Fig. 7) as a result of the substructure refinement of the bainitic packet (Fig. 3 and Table 2), and consequently σ_f was elevated.

Some previous works [24, 26–28] have focused on the microstructure-toughness correlation in martensitic/bainitic steels for revealing the effective microstructure unit. They reported that the martensitic/bainitic packet could serve as an effective microstructure unit controlling the impact properties due to their boundaries strongly impeding the crack propagation. Recently, You et al. [19, 28] reported a

tougher CGHAZ in high-strength pipeline steel by HAGBs including the bainitic packet boundaries. This attempt, therefore, presented an agreeable result with these previous works. By contrast, we determined the bainitic packet as the most effective microstructure unit governing the impact toughness of CGHAZ, via revealing the correlation of the bainitic packet with the cleavage facet, apart from their relations with FATT$_{50\%}$ and the impact fracture behavior.

5 Conclusions

1. The microstructure of simulated CGHAZ with different heat inputs mainly consisted of lath bainite. The bainitic packet/block/lath substructures were all refined significantly mainly due to the lowered A_{r3}, with the decreased heat input.
2. The impact toughness of simulated CGHAZ was enhanced significantly with the decreased heat input; each impact fracture surface exhibited typical cleavage morphologies, and the cleavage facet size decreased with the decrease in heat input.
3. The bainitic packet was the microstructural unit most effectively governing the impact properties in CGHAZ of X100Q steel, due to their close correlation with FATT$_{50\%}$, their size equivalent to the cleavage facet and their boundaries strongly impeding the crack propagation.

References

[1] S.Y. Shin, B. Hwang, S. Lee, N.J. Kim, S.S. Ahn, Mater. Sci. Eng. A 458 (2007) 281–289.
[2] W.G. Zhao, W. Wang, S.H. Chen, J.B. Qu, Mater. Sci. Eng. A 528 (2011) 7417–7422.
[3] C.L. Davis, J.E. King, Metall. Mater. Trans. A 25 (1994) 563–573.
[4] C. Ouchi, ISIJ Int. 41 (2001) 542–553.
[5] J. Chen, S. Tang, Z.Y. Liu, G.D. Wang, Mater. Sci. Eng. A 559 (2013) 241–249.
[6] J. Hu, L.X. Du, J.J. Wang, H. Xie, C.R. Gao, R.D.K. Misra, Mater. Sci. Eng. A 585 (2013) 197–204.
[7] P.C.M. Rodrigues, E.V. Pereloma, D.B. Santos, Mater. Sci. Eng. A 283 (2000) 136–143.
[8] D.S. Liu, B.G. Cheng, Y.Y. Chen, Metall. Mater. Trans. A 44 (2013) 440–455.
[9] S.C. Wang, P.W. Kao, J. Mater. Sci. 28 (1993) 5169–5175.
[10] R. Feng, S.L. Li, Z.S. Li, L. Tian, Mater. Sci. Eng. A 558 (2012) 205–210.
[11] E. Bonnevie, G. Ferrière, A. Ikhlef, D. Kaplan, J.M. Orain, Mater. Sci. Eng. A 385 (2004) 352–358.
[12] S.M. Zhang, K. Liu, H. Chen, X.P. Xiao, Q.F. Wang, F.C. Zhang, Mater. Sci. Eng. A 651 (2016) 951–960.
[13] Y.L. Kang, Q.H. Han, X.M. Zhao, M.H. Cai, Mater. Des. 44 (2013) 331–339.
[14] J. Hu, L.X. Du, J.J. Wang, C.R. Gao, Mater. Sci. Eng. A 577 (2013) 161–168.
[15] Z. Gao, R. Wei, K.M. Wu, Adv. Mater. Res. 538–541 (2012) 2026–2031.
[16] R.T. Li, X.R. Zuo, Y.Y. Hu, Z.W. Wang, D.X. Hu, Mater. Charact. 62 (2011) 801–806.
[17] A. Lambert-Perlade, A.F. Gourgues, A. Pineau, Acta Mater. 52 (2004) 2337–2348.
[18] A.M. Guo, R.D.K. Misra, J.B. Liu, L. Chen, X.L. He, S.J. Jansto, Mater. Sci. Eng. A 527 (2010) 6440–6448.
[19] Y. You, C.J. Shang, L. Chen, S. Subramanian, Mater. Des. 43 (2013) 485–491.
[20] H.K. Sung, S.Y. Shin, W. Cha, K. Oh, S. Lee, N.J. Kim, Mater. Sci. Eng. A 528 (2011) 3350–3357.
[21] Z.X. Zhu, M. Marimuthu, L. Kuzmikova, H.J. Li, F. Barbaro, L. Zheng, M.Z. Bai, C. Jones, Sci. Technol. Weld. Join. 18 (2013) 45–51.
[22] S. Morito, H. Tanaka, R. Konishi, T. Furuhara, T. Maki, Acta Mater. 51 (2003) 1789–1799.
[23] C. Garcia-Mateo, L. Morales-Rivas, F.G. Caballero, D. Milbourn, T. Sourmail, Metals 6 (2016) 130.
[24] H.J. Hu, G. Xu, M.X. Zhou, Q. Yuan, Metals 6 (2016) 173.
[25] S. Lee, B.C. Kim, D.Y. Lee, Scripta Metall. 23 (1989) 995–1000.
[26] Y.M. Kim, S.K. Kim, Y.J. Lim, N.J. Kim, ISIJ Int. 42 (2002) 1571–1577.
[27] J. Nohava, P. Haušild, M. Karlik, P. Bompard, Mater. Charact. 49 (2002) 211–217.
[28] Y. You, C.J. Shang, W.J. Nie, S. Subramanian, Mater. Sci. Eng. A 558 (2012) 692–701.
[29] C.Y. Zhang, Q.F. Wang, J.X. Ren, R.X. Li, M.Z. Wang, F.C. Zhang, K.M. Sun, Mater. Sci. Eng. A 534 (2012) 339–346.
[30] F.J. Barbaro, Z. Zhu, L. Kuzmikova, H. Li, J.M. Gray, in: 2nd International Symposium on Nb and Mo Alloying in High Performance Steels, Shanghai, China, 2013, pp. 1–13.
[31] X.L. Wang, Z.Q. Wang, L.L. Dong, C.J. Shang, X.P. Ma, S.V. Subramanian, Mater. Sci. Eng. A 704 (2017) 448–458.
[32] H.K.D.H. Bhadeshia, J.W. Christian, Metall. Trans. A 21 (1990) 767–797.
[33] C.W. Li, Y. Wang, T. Han, B. Han, L.Y. Li, J. Mater. Sci. 46 (2011) 727–733.
[34] S. Moeinifar, A.H. Kokabi, H.R. Madaah Hosseini, Mater. Des. 31 (2010) 2948–2955.
[35] S. Shanmugam, N.K. Ramisetti, R.D.K. Misra, J. Hartmann, S.G. Jansto, Mater. Sci. Eng. A 478 (2008) 26–37.
[36] T. Furuhara, H. Kawata, S. Morito, T. Maki, Mater. Sci. Eng. A 431 (2006) 228–236.
[37] H.K.D.H. Bhadeshia, Mater. Sci. Eng. A 273–275 (1999) 58–66.
[38] L.Y. Lan, C.L. Qiu, D.W. Zhao, X.H. Gao, L.X. Du, Mater. Sci. Eng. A 529 (2011) 192–200.
[39] J. Daigne, M. Guttmann, J.P. Naylor, Mater. Sci. Eng. 56 (1982) 1–10.
[40] I.A. Yakubtsov, P. Poruks, J.D. Boyd, Mater. Sci. Eng. A 480 (2008) 109–116.
[41] Y. Fukada, Y. Komizo, Trans. Jpn. Weld. Soc. 23 (1992) 3–10.
[42] H. Terasaki, Y. Shintome, A. Takada, Y. Komizo, K. Moriguchi, Y. Tomio, Metall. Mater. Trans. A 45 (2014) 3554–3559.
[43] M. Olasolo, P. Uranga, J.M. Rodriguez-Ibabe, B. López, Mater. Sci. Eng. A 528 (2011) 2559–2569.
[44] M.C. Zhao, K. Yang, F.R. Xiao, Y.Y. Shan, Mater. Sci. Eng. A 355 (2003) 126–136.
[45] S.C. Wang, J.R. Yang, Mater. Sci. Eng. A 154 (1992) 43–49.
[46] J.P. Naylor, P.R. Krahe, Metall. Trans. A 6 (1975) 594.